AGU PUBLICATIONS

JGR

Journal of Geophysical Research: Solid Earth

RESEARCH ARTICLE
10.1002/2017JB014434

A Geophysical Model for the Origin of Volcano Vent Clusters in a Colorado Plateau Volcanic Field

Fanghui Deng[1], **Charles B. Connor**[1], **Rocco Malservisi**[1], **Laura J. Connor**[1], **Jeremy T. White**[1], **Aurelie Germa**[1], **and Paul H. Wetmore**[1]

[1] School of Geosciences, University of South Florida, Tampa, FL, USA

Key Points:
- Volcanic vent clusters in the Springerville volcanic field coincide with lateral changes in crustal density, interpreted as transitions in the lithology of Proterozoic crust
- The origin of vent clusters is explained with a simple magma transport model using crustal density to constrain magma diffusivity and by comparing computed magma flux with the spatial density of mapped volcanoes
- Development of vent clusters in Quaternary Colorado Plateau volcanic fields appears to be influenced by large-scale lithologic variation in Proterozoic crust

Supporting Information:
- Supporting Information S1
- Data Set S1

Correspondence to:
F. Deng,
fanghuideng@mail.usf.edu

Citation:
Deng, F., Connor, C. B., Malservisi, R., Connor, L. J., White, J. T., Germa, A., & Wetmore, P. H. (2017). A geophysical model for the origin of volcano vent clusters in a Colorado Plateau volcanic field. *Journal of Geophysical Research: Solid Earth, 122*, 8910–8924. https://doi.org/10.1002/2017JB014434

Received 12 MAY 2017
Accepted 10 OCT 2017
Accepted article online 16 OCT 2017
Published online 11 NOV 2017

Abstract Variation in spatial density of Quaternary volcanic vents, and the occurrence of vent clusters, correlates with boundaries in Proterozoic crust in the Springerville volcanic field (SVF), Arizona, USA. Inverse modeling using 538 gravity measurements shows that vent clusters correlate with gradients in the gravity field due to lateral variation in crustal density. These lateral discontinuities in the crustal density can be explained by boundaries in the North American crust formed during Proterozoic accretion. Spatial density of volcanic vents is low in regions of high-density Proterozoic crust, high in areas of relatively low density Proterozoic crust, and is greatest adjacent to crustal boundaries. Vent alignments parallel these boundaries. We have developed 2-D and 3-D numerical models of magma ascent through the crust to simulate long-term, average magma migration that led to the development of vent clusters in the SVF, assuming that a viscous fluid flow through a porous media is statistically equivalent to magma migration averaged over geological time in the full field scale. The location and flux from the uniform magma source region are boundary conditions of the model. Changes in model diffusivity, associated with changes in the bulk properties of the lithosphere, can simulate preferential magma migration paths and alter estimated magma flux at the surface, implying that large-scale crustal structures, such as inherited tectonic block boundaries, influence magma ascent and clustering of volcanic vents. Probabilistic models of volcanic hazard for distributed volcanic fields can be improved by identifying crustal structures and assessing their impact on volcano distribution with the use of numerical models.

1. Introduction

We propose and test a model for the origin of vent clusters in the Springerville volcanic field (SVF), AZ. Distributed volcanic fields like the SVF are remarkable features, found in a variety of tectonic settings on Earth and nearby planets, with individual fields comprising tens to hundreds of volcanoes scattered across thousands of square kilometers (Addington, 2001; Hasenaka & Carmichael, 1985; Richardson et al., 2013; Williams, 1950). Often, volcanoes within these fields are thought to be monogenetic, with each volcano, or alignment of nearby volcanoes, representing a single, relatively short-lived magmatic event, such as intrusion of a dike swarm and eruption (Nakamura, 1977; Rittmann, 1962). On Earth, these volcanic fields are predominantly basaltic in composition, although many are bimodal (Bacon, 1982; Mazzarini et al., 2004). Most volcanoes within these distributed fields are scoria cones, small shields, or lava domes (Kereszturi & Németh, 2016; Valentine & Connor, 2015).

Distribution of vents within volcanic fields has been analyzed to delineate trends in volcanic activity, such as migration of the field with lithospheric plate motion (e.g., Condit et al., 1989; Tanaka et al., 1986), to better understand the relationship of volcanoes to prominent tectonic boundaries or faults (e.g., Conway et al., 1997; Heming, 1980; Kiyosugi et al., 2010; van den Hove et al., 2017), and to better assess the likely locations of future eruptions (Cappello et al., 2012; Connor et al., 2012). Statistical analyses of vent distribution have shown that volcanoes cluster within many distributed volcanic fields, rather than being randomly or regularly distributed (Bebbington, 2013; Le Corvec et al., 2013). For example, vent clusters are found in the subduction zone boundary of the Michoacán-Guanajuato volcanic field, Mexico (Connor, 1990), the SVF and San Francisco volcanic field (SFVF) on the margin of the Colorado Plateau (USA) (Condit & Connor, 1996; Conway et al., 1998), the rift-hosted Eifel volcanic field, Germany (Jaquet & Carniel, 2006; Schmincke et al., 1983), and farther from active plate boundaries (Cas et al., 2016; van den Hove et al., 2017; Wei et al., 2003).

The origin of vent clusters within distributed volcanic fields remains uncertain. One model is that magma source regions are heterogenous (e.g., Awdankiewicz et al., 2016), with some areas of the mantle more prone to partial melting than others leading to more frequent and voluminous activity in some parts of the field compared to others, a mechanism previously invoked to explain vent clusters in the SVF (Condit & Connor, 1996). Alternatively, the crust may act as a filter. Structures such as folds (e.g., Wetmore et al., 2009) and faults (e.g., van den Hove et al., 2017) may alter magma ascent pathways. Density discontinuities or rigidity contrasts in one part of the crust may tend to enhance sill formation and arrest dike ascent (e.g., George et al., 2016; Kavanagh et al., 2006) also a mechanism invoked to explain SVF volcanism (Putirka & Condit, 2003).

We explore the role of ancient lateral discontinuities in the crust beneath the SVF in changing patterns of volcanic activity. By re-examining the distribution of volcanic vents in the SVF and by comparing vent distribution to gravity anomalies that we have mapped across and around the field, lateral discontinuities in crustal density are identified, which are interpreted to have arisen during the accretion of the North American continent approximately 1.5 Ga ago (Gilbert et al., 2007).

Since it is practical to model the statistical distribution of vents mapped in the field as a continuous density function using kernel density estimation (Connor & Connor, 2009; Connor & Hill, 1995; Germa et al., 2013), we compare the SVF vent density distribution with a model of bulk magma transport, also formulated as a continuous distribution. Bulk magma transport is approximated using the advection-diffusion equation, with ascent from a uniform magma source region and with heterogeneity within the crust that alters flow paths and gives rise to variations in magma flux at the surface. A three-dimensional (3-D) gravity inversion (White et al., 2015) is used to delineate the most prominent lateral changes in crustal density, hence constraining the magma transport model.

We find that by using density discontinuities derived from the gravity data, the bulk magma transport model can simulate the major features of vent distribution observed in the SVF. That is, vent clusters, vent alignments, and overall changes in Quaternary vent distribution in the volcanic field are explained by the occurrence of lateral discontinuities in crustal properties that developed during the Proterozoic.

2. SVF Background

The SVF sits at the southern margin of the Colorado Plateau (Figure 1a). Magmatism at this margin is thought to result from asthenospheric convection, caused by the lithospheric drip from the base of the plateau, which is metasomatized and heated (Van Wijk et al., 2010). These magmas pass through Proterozoic crust during ascent. Knowledge of the composition of this Proterozoic crust derives primarily from extensive exposures to the southwest of the Colorado Plateau in what is known as Arizona's transition zone. Studies of the Proterozoic rocks exposed within this transition between the Colorado Plateau and the Basin and Range Province to the southwest have resulted in the identification of several structural blocks that are characterized by contrasting compositions and different structural and magmatic evolutions. The boundaries between the blocks trend northeast and thus suggest that the blocks can be extrapolated northeastward into the Colorado Plateau. The SVF is located south of the Slate Creek shear zone and at the southern end of the Jemez Lineament near the center of the Sunflower Block (Anderson et al., 1993; Karlstrom & Bowring, 1988; Karlstrom & Williams, 2006) (Figure 1a). The composition of the Sunflower Block is dominated by a suite of 1640 – 1630 Ma granitic intrusive rocks, with a few exposures of high-grade metasedimentary rocks and some younger 1400 Ma granitic rocks that are concentrated along the southeastern boundary (Karlstrom & Bowring, 1988). Gravity and magnetic anomalies, as well as structural and geochemical mapping of the region, show that these broad lithologic transitions in the Proterozoic crust are preserved today, primarily creating NE-SW trending gravity (Figure 1b) and magnetic anomalies that parallel shear zones (faults) mapped at the surface, which have been intermittently activated, for example, in Laramide orogeny (Seeley & Keller, 2003; Shoemaker et al., 1978). These investigations have also identified WNW-ESE trending structures in the basement, interpreted to be associated with Proterozoic extension (Seeley & Keller, 2003). Regional gravity anomalies show that both trends in gravity gradients occur around the SVF, suggesting that these Proterozoic-aged lithologic boundaries extend across the field. The Proterozoic boundaries are largely masked at the surface in the SVF by Paleozoic sedimentary rocks. Crumpler et al. (1994), however, mapped monoclinal flexures and faults in the SVF that have predominantly WNW-ENE orientations (Figure 2), suggesting that Proterozoic boundaries localized later deformation.

Spatial distribution of calc-alkaline volcanic rocks of mid-Cenozoic age suggests that a low-angle subduction of the Farallon plate during the Laramide orogeny persisted until the early Miocene (Thompson & Zoback, 1979).

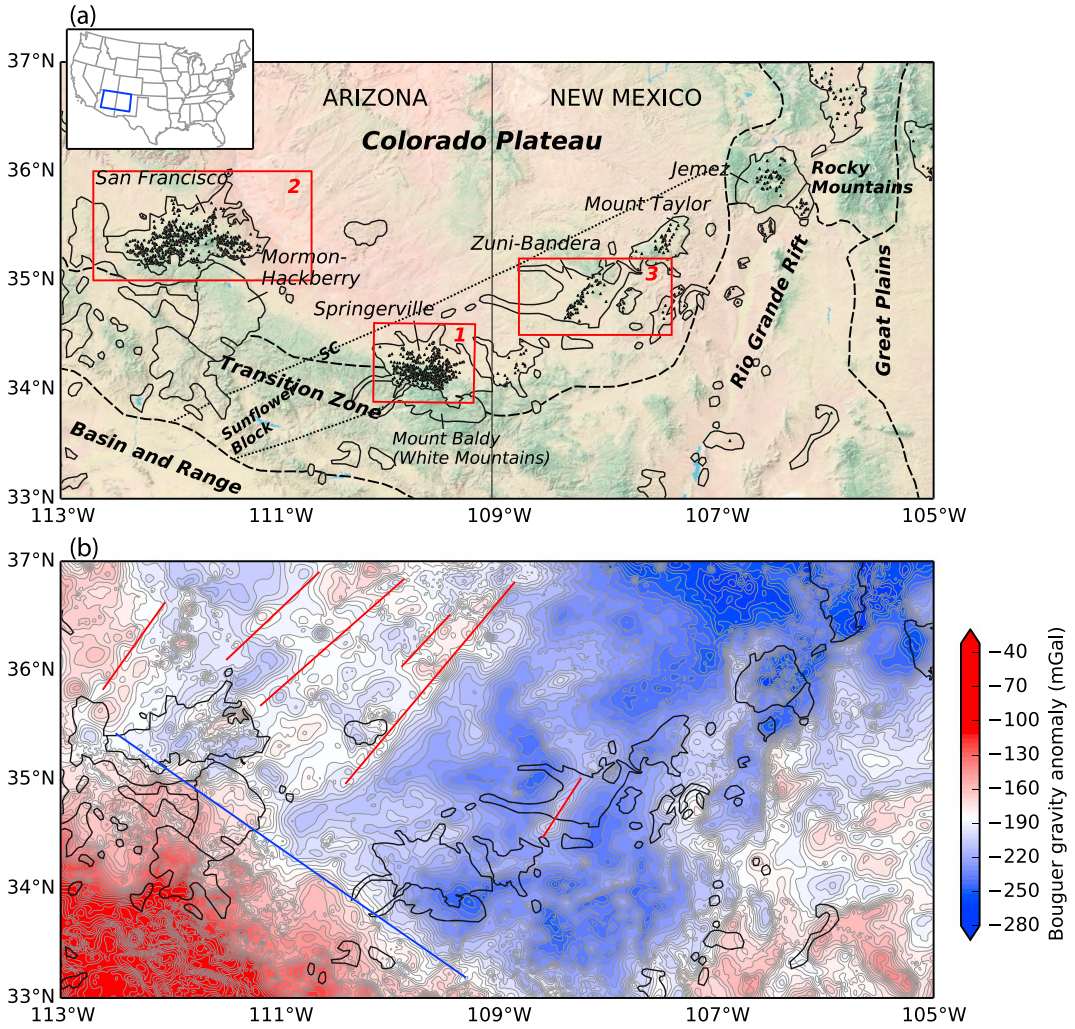

Figure 1. (a) Numerous volcanic fields are located near the southern margin of the Colorado Plateau, including Springerville (SVF), San Francisco (SFVF), Zuni-Bandera, Mount Taylor, Jemez, and Mormon-Hackberry (from Luedke & Smith, 1978, outlined on this shaded relief digital elevation model. Black dashed lines mark the borders of the Colorado Plateau, the Arizona transition zone, the southern Basin and Range, the Rio Grande Rift, the southern Rocky Mountains, and the Great Plains. The Slate Creek shear zone (SC) and the Sunflower Block (from Karlstrom & Bowring, 1988; Karlstrom & Williams, 2006) are indicated with black dotted lines. The Jemez lineament (Aldrich & Laughlin, 1984) west of the Great Plains extends SW from the Jemez volcanic field, through the Mount Taylor, Zuni-Bandera, and Springerville volcanic fields. Small black triangles are Quaternary volcanic vents. Red boxes indicate the (1) SVF, (2) SFVF, and (3) Zuni-Bandera volcanic fields. (b) Complete Bouguer gravity anomaly map of the southern Colorado Plateau. Gravity data are from the UTEP database (University of Texas at El Paso (UTEP) database, 2017); contour interval is 4 mGal. Note prominent gravity gradients trend NE-SW (red lines), while in the transition zone prominent gravity gradients trend WNW-ESE (blue line).

The lithospheric mantle directly overlying the slab was hydrated and consequently weakened (Dixon et al., 2004; Humphreys et al., 2003). Subsequent deepening and removal of the Farallon slab resulted in downwelling of the weakened lithosphere, which was progressively replaced by an asthenospheric flow (Crow et al., 2011; Dixon et al., 2004; Humphreys, 1995; Humphreys et al., 2003; Levander et al., 2011; Thompson & Zoback, 1979; Van Wijk et al., 2010; Zandt et al., 2011). Expansion of the lithosphere caused elevation of mantle isotherms and initiated mantle melting during the middle to late Miocene on the western and southeastern plateau margins corresponding to the Arizona transition zone (Condit et al., 1989; Crow et al., 2011). This initial stage of vigorous upwelling caused extensive melting of a lithospheric mantle source, while later waning heat supply resulted in a lower degree of partial melting (Condit et al., 1989). Alkali basalts that erupted within volcanic fields in the transition zone have signatures showing evidence of mixing between depleted asthenospheric and enriched lithospheric mantle melts (Cooper & Hart, 1990).

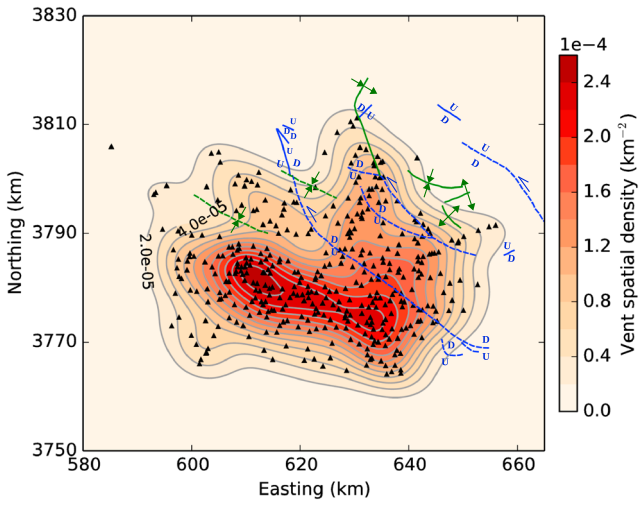

Figure 2. Spatial density map of Quaternary volcanic vents (black triangles) of the SVF (see red box 1, Figure 1a). There are multiple modes (clusters) in vent distribution shown in the spatial density. The most prominent clusters form a WNW trending band. Gray lines are contours of vent density with interval 2.0×10^{-5} km^{-2}. Flexures are drawn in green; normal (D/U) and strike-slip (⇀) faults are from Crumpler et al. (1994). UTM coordinates (zone 12°N, as in the rest of the paper) are given at the margin.

The SVF is the southernmost of these Colorado Plateau margin volcanic fields. It stands out from most neighboring fields (e.g, SFVF) by lacking a silicic or composite volcanic center. Miocene and Pliocene basalt lavas appear to be much more voluminous in the SVF region than subsequent Quaternary volcanism. Lavas from Mount Baldy shield volcano, located SE of the SVF (Figure 1a) and not considered part of the SVF, have radiometric age determinations of 8.7 ± 0.2 Ma and 9.0 ± 0.2 Ma (Condit, 1984; Condit & Shafiqullah, 1985; Nealey, 1989). Much of the Quaternary SVF products erupted onto an older lava flow surface consisting of tholeiites to hawaiites ranging in age from 7.6 ± 0.4 Ma to 2.9 ± 0.1 Ma (Condit & Connor, 1996; Laughlin et al., 1980). The SVF lavas consist of 24% tholeiites (circa 2.1–0.3 Ma), generally followed by alkali olivine (47% of the erupted volume) and evolved alkali rocks (hawaiite, 28% and mugearite and benmoreite, <1%) emplaced between circa 1.75 and 0.3 Ma (Aubele et al., 1986; Condit & Connor, 1996; Condit & Shafiqullah, 1985; Cooper & Hart, 1990; Peirce et al., 1979). Thus, the SVF region has experienced episodic volcanism since approximately 9 Ma ago, with chemical heterogeneity in the basaltic magmas erupted. Major, trace, and isotopic chemical analyses reveal that tholeiitic basalts were generated by a lithospheric mantle source, similar to an EMI-type (enriched mantle type I) reservoir that later slightly interacted with a crustal component (Cooper & Hart, 1990). In contrast, alkali lavas were generated in a depleted asthenospheric mantle (PREvalent-MAntle-type, similar to Northern Hemisphere oceanic island basalts) that mixed with a metasomatized lithospheric mantle source (EMI-type) and an high μ (HIMU)-type source with radiogenic Pb (Cooper & Hart, 1990). The HIMU-type source derives from the recycling of an ancient oceanic crust inherited from the Late Cretaceous to early Tertiary subduction (Cooper & Hart, 1990). No spatial migration of lava composition has been identified, implying that there were minimal thermal changes in the source region during Quaternary activity (Condit et al., 1989). The available geochemical data are not enough to constrain the spatiotemporal evolution of vent distribution, which is also complicated by additional factors, including regional structure (Connor et al., 1992).

Analysis of clinopyroxene-whole-rock pairs in SVF basalts were used to derive pressure and temperature of crystallization and indicate that magmas originate at a wide range of depths, up to at least 60 km (Putirka & Condit, 2003). Significantly, some relatively high K_2O and K/Ti basalts appear to have stagnated at depths of 0–12 and 23–30 km, within the Proterozoic section. No evidence of stagnation at the Moho (approximately 35 km deep) (Gilbert et al., 2007) was identified by Putirka and Condit (2003), suggesting that rheological boundaries within the crust impacted magma ascent in the SVF.

A total of 409 Quaternary vents and associated lava flows has been mapped in the SVF (Condit, 1984; Condit et al., 1989), which have been grouped into approximately 366 eruptive events, as some eruptions resulted in the construction of multiple vents and vent alignments (Condit & Connor, 1996). These vents form clusters; eruptive activity waxed and waned within clusters at much higher rates than in the field on average. The overall pattern of vent distribution is characterized by a broad WNW-trending band of volcanoes, roughly parallel to mapped flexures (Figure 2) and inferred Proterozoic lithologic boundaries. Vent alignments also tend to parallel to these boundaries (Connor et al., 1992). These observations suggested to us that the diverse geochemical features and the spatial clustering of volcanism in the SVF may be related to lateral changes in the Proterozoic crust that alters pathways of magma ascent.

3. Spatial Density of Volcanic Vents

Spatial intensity of volcanism (the number of events per unit area) and spatial density (the number of events per unit area normalized by the total number of events) reflect the probability of a volcanic eruption occurring at a specific location, given that eruptions occur within the volcanic field (Connor & Connor, 2009). Kernel density estimation is a statistical method defining the spatial density that results in a smooth and differentiable surface and so facilitates recognition of areas of significant vent clustering or unusually high vent density areas.

Spatial density of volcanic vents in the SVF is estimated with the kernel density estimation method developed by Connor and Connor (2009) and Germa et al. (2013). The spatial density estimate is based on a bivariate, Gaussian kernel function and a directional, two-dimensional (2-D) smoothing bandwidth to account for the directional distribution of vents within a volcanic field. For a given location ($\mathbf{s}$), the spatial density $\hat{\lambda}(\mathbf{s})$ is calculated using (Connor & Connor, 2009)

$$\hat{\lambda}(\mathbf{s}) = \frac{1}{2\pi N\sqrt{|\mathbf{H}|}} \sum_{i=1}^{N} exp\left[\frac{-1}{2}\mathbf{b}^T\mathbf{b}\right], \quad (1)$$

where N is the total number of volcanic vents, $\mathbf{H}$ is the bandwidth matrix, and $|\mathbf{H}|$ is the determinant of the matrix. $\mathbf{b} = \mathbf{H}^{-1/2}\mathbf{x}$, $\mathbf{x}$ is a 1×2 distance matrix specifying the distance from ($\mathbf{s}$) to each vent along N-S and E-W directions. $\mathbf{b}^T$ is the transpose of $\mathbf{b}$. The smoothing bandwidth of the SVF is estimated based on a mean integrated squared error approach (Wand & Jones, 1995). The bandwidth matrix is estimated using the smoothed asymptotic mean integrated squared error method for multivariate kernel smoothing (Duong, 2007).

The computer code used by Germa et al. (2013) was applied for the spatial density estimation of the SVF (Figure 2). Spatial density analysis primarily shows that vents cluster within the SVF, rather than being completely randomly distributed. The highest vent density ($\geq 1.8 \times 10^{-4}$ km^{-2}) occurs within a multimodal WNW trending cluster, as indicated by the deep red-orange shading on the map in Figure 2. Other vent clusters are visible around this main cluster, evident as undulations in contoured spatial density.

4. Collection and Modeling of Gravity Data

New gravity data were collected and added to the regional database (University of Texas at El Paso, 2017) to analyze the relationship between vent distribution and gravity anomalies, to identify lateral density contrasts in the crust across the field, and to provide constraints on magma diffusivity, a key parameter used to model magma flux.

4.1. Gravity Data Collection and Processing

We collected 279 new gravity data using a Burris gravimeter (B-38) with measurement precision of ≈0.002 mGal. Trimble CenterPoint RTX service (Leandro et al., 2011) with one Global Positioning System (GPS) R10 rover receiver was used to locate gravity stations. This relatively new technique gives ≈4 cm horizontal accuracy and ≈10 cm vertical accuracy without the requirement of a GPS base station (Leandro et al., 2011), corresponding to gravity measurement uncertainty of ≈0.03 mGal.

A gravity base station network was established across the volcanic field to correct gravimeter instrument drift. Free-air, latitude, atmospheric mass, Bouguer, and terrain corrections were applied to calculate the complete Bouguer anomaly (Blakely, 1996; Hammer, 1939; LaFehr, 1991). A reduction density of 2,670 kg/m^3 (Hinze, 2003) was used in the Bouguer and terrain corrections. A digital elevation model (DEM) with 10 m resolution provided by the 3-D elevation program (Sugarbaker et al., 2017) was used for terrain corrections within 20 m to 15 km around each gravity station, and a 90 m Shuttle Radar Topography Mission (SRTM) DEM (Farr et al., 2007) was used for terrain corrections from 15 km to 167 km. Terrain corrections for all gravity measurements range from 0.30 to 4.28 mGal. These new gravity measurements were combined with gravity measurements from the University of Texas at El Paso (UTEP) database.

The new gravity anomaly map refines the gravity gradients, especially in the east part of the field (Figures 3a and S1 in the supporting information). The gravity anomaly map is dominated by relatively high gravity anomalies in the northwest and low gravity anomalies in the southeast. The total gravity change in the NW-SE direction is approximately 40 mGal. The gravity gradient in the volcanic field is steepest in the central and northeast parts, with gradient commonly reaching 4 mGal/km (Figure S2b in the supporting information). The majority of volcanic vents in the SVF form a WNW-trending band that intersects the steepest gravity gradient where the gravity gradient changes trend from N-S to ENE. Volcanism continues to the WNW across the gravity gradient, but where this gradient is most subduded. The steepest gravity gradient bifurcates in the eastern portion of the field, forming gradients that trend for >30 km in ENE and NE directions, creating a nearly isolated gravity high (about easting 650 km and northing 3,795 km) in the eastern portion of the SVF. Volcano alignments are most obvious in the east and northeast parts of the field. These alignments coincide with and parallel the steep gravity gradients (Figure 3b). The amplitude and wavelength of the gravity change across the map is consistent with a major crustal boundary (Seeley & Keller, 2003). Conversely, the amplitude

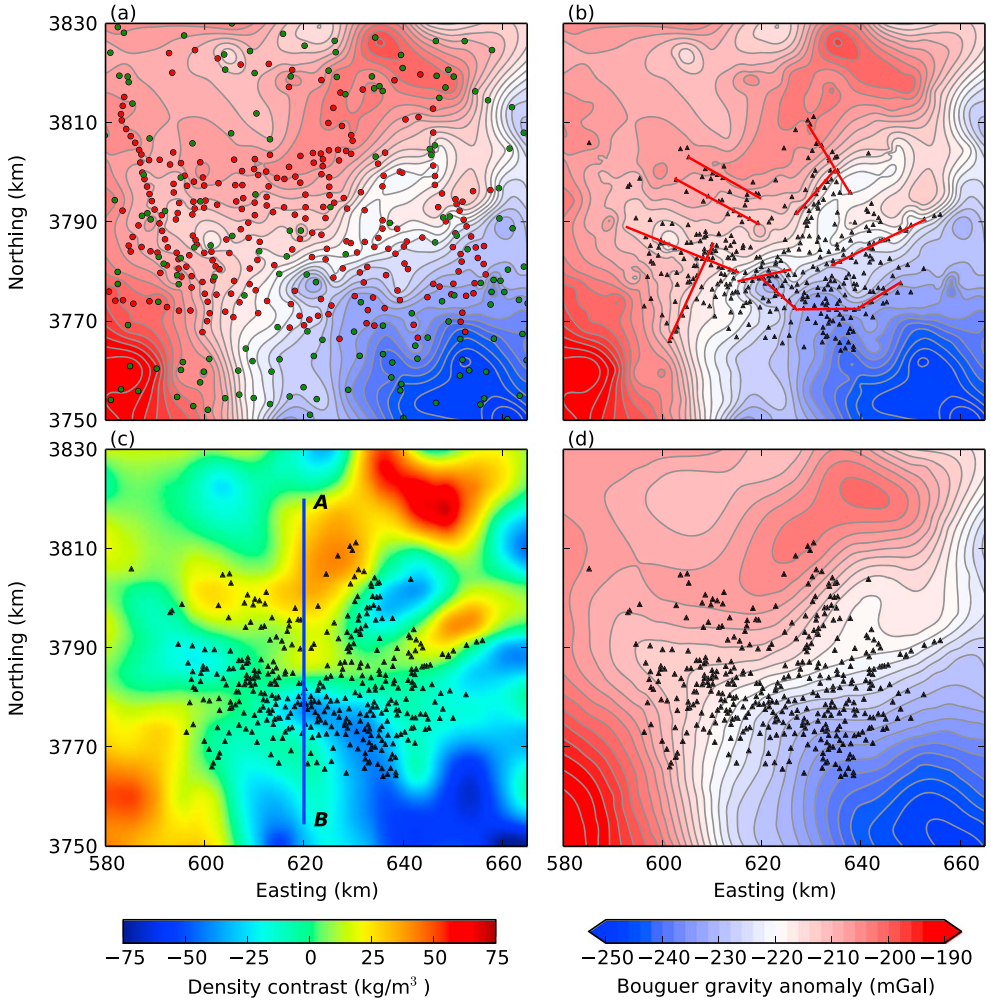

Figure 3. Complete Bouguer gravity anomaly map of the SVF gridded at a spacing of 0.5 km based on the minimum curvature algorithm using Generic Mapping Tools (GMT) software (Wessel et al., 2013). Contour interval is 2 mGal. (a) Red and green dots mark new and previous (UTEP database) gravity stations, respectively. (b) Black triangles are volcanic vents. Red lines are vent alignments from Connor et al. (1992). Note that NNE and ENE trending vent alignments correspond to the observed gravity gradients in the E and NE part of the field. (c) Inverted crustal density contrast resampled to 0.5 km by 0.5 km based on the minimum curvature algorithm. High vent density and vent alignments correspond to low crustal density and high crustal density gradient. Profile *AB* indicates the location of the 2-D model for magma transport (Figure 4). (d) Calculated gravity anomaly map with 0.5 km by 0.5 km resolution. The long-wavelength features of the observed gravity anomaly (Figure 3b) are captured by the calculated gravity anomaly (Figure 3d) based on the inverted density distribution (Figure 3c).

and wavelength of the gravity anomaly cannot be explained by comparatively local features, such as igneous intrusions (Figure S3), or by basin development, particularly because the Paleozoic section is flat lying across the map area. Nor can the comparatively thin veneer of lava flows that comprise the SVF explain the gravity anomaly. Instead, we attribute the gravity anomaly to broad density contrast preserved in the crust from the pre-Paleozoic.

4.2. Inversion for Density Contrast With PEST

The gravity data coupled with tectonic models of the region (Gilbert et al., 2007; Seeley & Keller, 2003) suggest a modeling strategy. There is no deformation of the Paleozoic or younger section on the southern Colorado Plateau, nor is there known variation in the depth to the Moho on the scale of the gravity map. Furthermore, the observed gravity gradient is too steep to be attributed to a lateral change in the depth to the Moho. Consequently, we focus on lateral changes in the density of the Proterozoic crust, which is consistent with regional gravity models (Seeley & Keller, 2003).

The density inversion model is created by subdividing the crust into a grid of rectangular prisms. Each prism is given some initial values: length, width, depth to top, depth to bottom, and a constant density value; this density value is the only value adjusted during the inversion process. The modeled gravity anomaly is calculated by summing the gravity contribution from each prism defined in the initial grid, after adjusting the density of each prism via inversion, so that the resulting calculated gravity anomaly map closely resembles the observed gravity anomaly map. The "forward" solution that calculates the gravity anomaly due to a grid of crustal prisms is based on the algorithm in Blakely (1996) and is more completely described in White et al. (2015).

All prisms extend from the base of the Paleozoic sedimentary overburden to the Moho. Sedimentary overburden in the SVF is about 2 km thick (Putirka & Condit, 2003). Based on seismic data, the Moho is approximately 35 km deep in the SVF (Gilbert et al., 2007). The top and bottom depth of each prism is therefore fixed at 2 km and 35 km, respectively. A total of 2,025 prims comprises the model. The initial prism grid is designed so that areas containing more gravity readings are modeled by a greater number of narrower prisms and areas with few gravity readings are modeled using wider prisms; this results in nonuniformity of the grid. The horizontal areas of prisms range from 1.1 km^2 to 57.0 km^2. Prisms extend several kilometers beyond the study area to reduce edge effects in the calculated gravity anomaly (Figure S4a in the supporting information).

Inversion is performed using the software package PEST (Model-Independent Parameter Estimation and Uncertainty Analysis), which combines singular value decomposition (SVD) and Tikhonov regularization (Doherty, 2016; White et al., 2015) to find a best fit density model. We have 2,025 unknown parameters (density contrasts) and 538 gravity observations (279 new measurements and 259 previous measurements). This problem is ill posed, since there are more unknown parameters than observations. SVD provides numerical stability to the ill-posed inverse problem. The first-order Tikhonov regularization assures that the density model varies smoothly. This regularization provides a way to constrain the solution with prior information, which in our case is that crustal density will not change abruptly.

Because we are most interested in the variation in density contrast (i.e., density difference between adjacent prisms), the average gravity anomaly was subtracted from the complete Bouguer anomaly before the inversion. Although the modeled density contrast of prisms varies from −137.9 kg/m^3 to +147.8 kg/m^3, the inversion indicates that most prisms have a narrower range of density contrast (−55 kg/m^3 to +55 kg/m^3), with peak value about 0 kg/m^3 (Figures 3c and S4b in the supporting information).

The modeled gravity anomaly has the long-wavelength features of the observed gravity anomaly (Figures 3d, S5, and S6 in the supporting information). Compared to the observed anomaly, the modeled anomaly is slightly smoothed. This smoothing relates to the dimensions and geometry of the model prisms and the use of the first-order Tikhonov regularization.

Inverse modeling of crustal density contrast verifies that volcano distribution appears to respond to lateral changes in crustal density (Figure 3c). Most volcanic vents are located in areas of relatively low modeled crustal density, and some volcano alignments appear to parallel transition zones from high to low crustal density. Although the inverted crustal density contrasts represent only the long-wavelength feature of the observed gravity anomaly, it is sufficient for our magma flow model, since we are most interested in the relationship between the long-term average magma migration and large-scale crustal structures.

5. Magma Transport Model

Putirka and Condit (2003) find that magma in the SVF is less dense than most of the crust. Buoyancy is not likely the main factor controlling vent distribution on the surface because high vent density (normalized volcanoes per square kilometer) occurs in areas of low crustal density (kg m^{-3}), that is, in areas of reduced lithostatic load and reduced buoyancy force. Thus, we do not suggest that volcano distribution is directly caused by lateral changes in crustal density. Instead, rocks with high density may also have high rigidity, or other changes in elastic properties, which may tend to enhance sill formation, arrest dike ascent or otherwise favor lateral flow (Kavanagh et al., 2006; Maccaferri et al., 2010, 2011).

Our goals for the magma transport model are to study the average behavior of magma migration over geological time and to relate the model result to the statistical model of vent spatial density. Thus, volcanoes and magma migration are not studied in terms of the complexities of dike injection, sill development,

or transient processes. Instead, we study the average of these processes over geologic time. Specifically, the magma transport model is used to investigate how lateral changes in crustal properties might alter magma migration through the crust and hence alter volcano density at the surface.

Using the ergodic hypothesis, a statistical equivalent of magma migration averaged over geological time can be approximated by the steady state flow of a viscous fluid within a porous medium (Bonafede & Boschi, 1992; Bonafede & Cenni, 1998). Using this assumption, the advection-diffusion equation describing magma migration in the lithosphere is equivalent to Darcy's law. The mathematical model of 3-D movement of the magma (viscous fluid) through the lithosphere (porous medium) can be described by the partial-differential equation (modified from Schwartz & Zhang, 2003, and Harbaugh, 2005):

$$\frac{\partial}{\partial x}\left(K_x\frac{\partial m}{\partial x}\right)+\frac{\partial}{\partial y}\left(K_y\frac{\partial m}{\partial y}\right)+\frac{\partial}{\partial z}\left(K_z\frac{\partial m}{\partial z}\right)+Q=\frac{\partial m}{\partial t}, \tag{2}$$

where K_x, K_y, and K_z are magma diffusivities in horizontal (x, y) and vertical (z) directions; m is the volume of magma per unit area; Q is the volumetric flux per unit area; and t is time. SI units for K, m, Q, and t are m^2/s, m, m/s and s, respectively. In general, K_x, K_y, K_z, and Q are functions of space and time, but in this steady state model they are taken as constant in time.

Magma diffusivities K_x, K_y, and K_z represent the relative ease with which the magma moves in 3-D space, with higher diffusivity indicating relatively easier magma movement. We emphasize that the value of diffusivity is not a physical property of magma or lithosphere. Instead, diffusivity is a model parameter that describes bulk behavior, the average ability of the lithosphere to transport magma over geological time. Variability in diffusivity of the lithosphere represents multiple factors that may influence magma transport, including the presence of fractures, varying lithology, density, rigidity, thermal state, and/or regional stresses. Mathematically, diffusivity acts as a filter describing how a uniform magma source region at depth manifests as distributed volcanism at the surface.

Finite-difference methods are often used to provide numerical solutions to equation (2). We use MODFLOW software (Harbaugh, 2005), a 3-D finite-difference groundwater model, to simulate the migration of magma in the lithosphere. The continuous real-world system is represented by a grid of blocks with nodes at the center of each cell. The differences in m at these nodes replace the partial derivatives in equation (2).

Taking the integration of the Quaternary volcanism at the surface of the SVF, our magma transport model is in steady state condition. That is, the model will converge when the sum of magma inflow and outflow is zero for each cell. When the system reaches steady state, m for each cell does not change with time, which means $\frac{\partial m}{\partial t}=0$. The source term, Q, represents a homogeneous magma source, which is located at the lithosphere-asthenosphere boundary (LAB) in our model. No other magma sources are considered.

The diffusivity in our model domain is anisotropic and heterogeneous. The vertical diffusivity (K_z) is higher than the horizontal diffusivity (K_x and K_y). This reflects the tendency for magmas to rise buoyantly. In this model we assume that $K_x = K_y$, considering that deviatoric stress on the Colorado Plateau is relatively low (Heidbach et al., 2010). We assume that diffusivity varies from place to place in the SVF, in order to model the clustered nature of volcanism assuming a uniform magma source region.

To achieve the simplest approximation, we convert crustal density contrasts derived from the gravity inversion to vertical diffusivities in the crust, assuming a linear model:

$$K_{zc}=\frac{\Delta\rho_{\max}-\Delta\rho}{\Delta\rho_{\max}-\Delta\rho_{\min}}\times K_{zm}\times N_1\times N_2, \tag{3}$$

where $\Delta\rho$ is the crustal density contrast in a given model grid cell. $\Delta\rho_{\max}$ is the maximum crustal density contrast. $\Delta\rho_{\min}$ is the minimum crustal density contrast. K_{zm} is the vertical diffusivity in the mantle lithosphere. K_{zc} is the vertical diffusivity in the crust (2 km–35 km). K_{zm} is a constant for the whole mantle lithosphere in our model. That is, the model mantle lithosphere is homogeneous. K_{zc} varies with different density contrasts. High-density contrasts correspond to low diffusivities. Low-density contrasts correspond to high diffusivities. N_1 is the ratio between the highest vertical diffusivity in the crust and K_{zm}. N_2 is the ratio between vertical

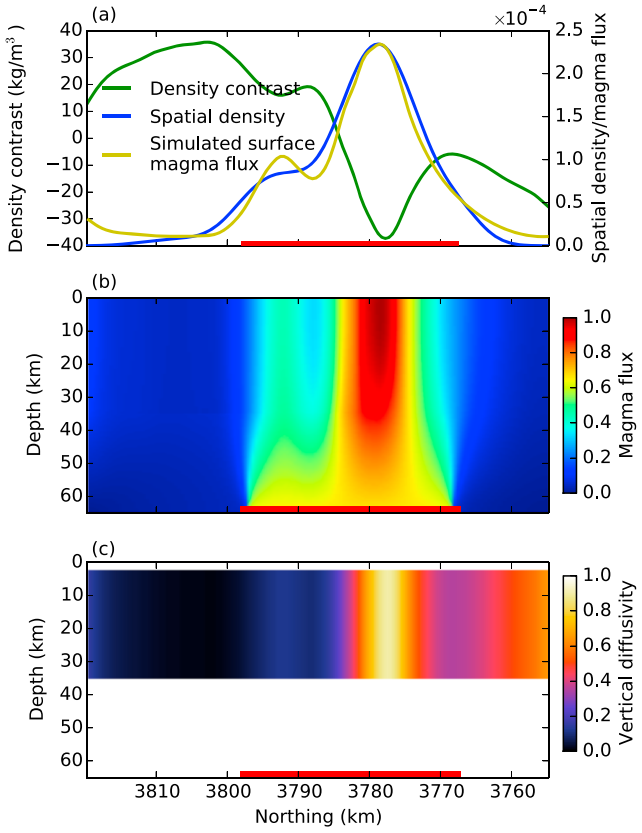

Figure 4. Simulated magma flux and vertical diffusivities of the 2-D model (profile location shown in Figure 3c). Red lines on the horizontal axes indicate the location of magma source at the LAB. (a) Comparison between crustal density contrasts (green line), vent spatial density (blue line), and simulated magma flux at the surface (yellow line, rescaled to vent spatial density). The main features of vent density, a principle peak with a moderate shoulder, are captured by the simulated surface magma flux. The maximum vent density is near a local minimum crustal density contrast and adjacent to the steepest crustal density gradient. (b) Simulated magma flux of the whole model domain shown in profile from the LAB to surface. (c) Vertical diffusivities constrained by density contrasts from the LAB to surface.

and horizontal diffusivities. N_1 and N_2 are set to be constant in our model and are determined by parameter sensitivity analysis.

Boundary conditions used in our model are (1) the magma source is located at the deepest layer of the model and has constant flux and (2) the top layer has a constant volume of magma per unit area, $m = 0$. The magma source flux and diffusivities do not change with time. Seismic data suggest that the LAB is about 65 km deep (Liu et al., 2011). In all simulations, the vertical extent of our model domain is 0 km (surface) to 65 km (LAB). The magma source is simulated by the Well Package in MODFLOW. The source "pumps" magma into the system via the bottom layer continuously. One model output is simulated magma flux at the surface. By varying diffusivities anywhere within the crust, the simulated surface magma flux changes. Because we are interested in relative change in diffusivity and its influence on volcano clustering, diffusivities and simulated magma flux are normalized to (0, 1]. Both 2-D and 3-D modeling of bulk magma transport are discussed in the following.

5.1. Two-Dimensional Model Results

In 2-D, the surface magma flux is simulated along profile *AB* (UTM easting 620 km, Figure 3c and 4a). The extent of this 2-D model is UTM northing 3,755 km to 3,820 km and from the surface to 65 km depth (Figures 4b and 4c). This model space is subdivided into a 130 × 130 grid; each cell is 0.5 km in both width and depth. The horizontal extent of the magma source region at the base of the model domain is determined by the footprint of volcanic vents. The extent of source region and horizontal diffusivites affect the lateral distribution of surface magma flow. The amount of magma reaching the surface at different locations is controlled by the distance to the source center and diffusivities along magma pathways. The mantle lithosphere and sedimentary overburden are assumed to be homogeneous, while the remaining crust is heterogeneous. The vertical diffusivity in the crust was constrained by the crustal density contrast in our model (equation (3). The highest vertical diffusivity in the crust is $K_{zm} \times N_1 \times N_2$. For all model cells, the vertical diffusivity is N_2 times greater than the horizontal diffusivity. Thus, the values of N_1 and N_2 are adjusted to match the simulated surface magma flux and the spatial density of volcanic vents. Parameter sensitivity analysis indicates that $N_1 = 1$ and $N_2 = 150$ are a reasonable parameter combination (Figures S7 and S8 in the supporting information).

The main feature of vent density along this N-S profile is a maximum near UTM northing 3,780 km (Figure 4a). This area corresponds to a local crustal density minimum. The maximum in vent density is just south of a local steepest gradient in modeled crustal density contrast. Vent density also has an elevated shoulder north of the maximum, extending 5 km north to the edge of the SVF, about UTM northing 3,795 km on the profile line. This shoulder of relatively high vent density corresponds to lower crustal densities than are found farther north along the profile. This step in crustal density, mirrored in the vertical diffusivity, allows this detail of the vent density to be modeled.

An important feature of the profile *AB* is that vent density cannot be modeled simply by correlating directly to crustal density. Relatively low crustal densities are located at the south of the profile and relatively high vent densities are 15–20 km north of this area. Rather, it is necessary to map crustal density into vertical diffusivity and to model the change in magma flux. This step is necessary because ascending magma in the northern part of the profile is redirected southward by the variation in diffusivity. This causes a maximum in spatial density a few kilometers south of the steepest gradient in crustal density. Such a maximum is not explained by correlating with crustal density contrast alone, because this parameter cannot account for the redirection of ascending magma.

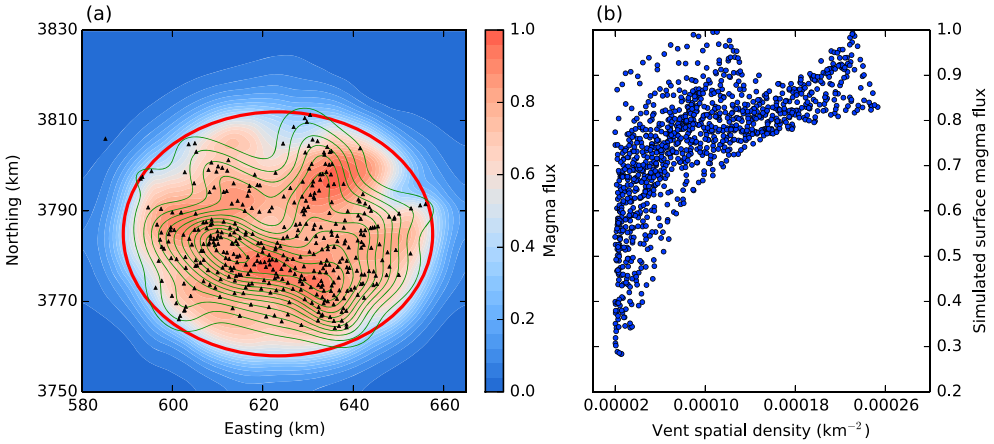

Figure 5. (a) Variation in simulated magma flux at the surface based on the 3-D magma transport model. The red ellipse shows the lateral extent of a uniform magma source region at the LAB. Variable magma diffusivity in the crust, derived from density contrast found by gravity inversion (Figure 3c), creates variation in simulated magma flux at the surface (color shading). Areas of higher magma flux based on this simulation correspond to mapped vent clusters (black triangles) and high spatial vent density (green contours as in Figure 2). (b) Scatterplot of vent spatial density and the simulated surface magma flux at locations where vent density is not less than 2.0×10^{-5} km^{-2} (Figures 2 and S9a). The concentrated dots show that the vent density has a positive correlation with the simulated magma flux. Figures 5a and 5b suggest that lateral variation in crustal properties is responsible for vent clustering in the SVF. It is necessary to remap crustal density into vertical diffusivity and to model the change in magma flux (Figure S9).

5.2. Three-Dimensional Model Results

For the 3-D modeling, the extent of our model is 580 km to 665 km in UTM easting, 3,750 km to 3,830 km in UTM northing (Figure 5a), and 0 km to 65 km in vertical depth. This model volume is divided into a 160×170 grid with 130 layers. Each cell is 0.5 km in width, length, and height. The magma source area at the base of this model is elliptical in horizontal dimension. The extent of the source is determined by the footprint of volcanic vents mapped at the surface. As in the 2-D case, equation (3) is used to convert density contrasts derived from the gravity inversion to vertical diffusivities in the crust; the same values of N_1 and N_2 used in the 2-D model are applied in the 3-D model. Vent density and simulated surface magma flux are compared in Figures 5a and 5b.

The main features of the vent density are captured by the simulated magma flux (Figure 5a). Most importantly, the multimodal WNW trending band in high vent density is simulated by the 3-D magma transport model. Smaller vent clusters in the northern half of the field are also simulated by the model, as well as gaps in vent density distribution. As in the 2-D model, maximum flux in the magma transport model does not correspond exactly to areas of the lowest crustal density contrast or highest diffusivity. Instead, high simulated magma flux occurs where magma is redirected around low vertical diffusivity zones.

The positive correlation between vent density and simulated magma flux (Figure 5b) suggests that lateral variation in crustal properties is responsible for the vent clustering in the SVF. It is necessary to remap crustal density into vertical diffusivity and to model the change in magma flux (Figure S9). The sharp lower bound in Figure 5b is both model and data related. High vent density is not likely to happen in areas with high crustal density (Figure 2) in the SVF. This is indicated by a relatively sharp high bound in the distribution map of vent density and crustal density contrast (Figure S9c). In our model, the low diffusivity is related with the high crustal density. Therefore, with a uniform magma source, the simulated magma flux will not be low at areas with high vent density.

6. Discussion

The relatively high crustal density zones identified by modeling gravity data are possibly greenstones and related rocks associated with Proterozoic island arcs. In contrast, lower density areas may be composed of more silicic crust, including Proterozoic basin sequences that were remobilized and deformed during

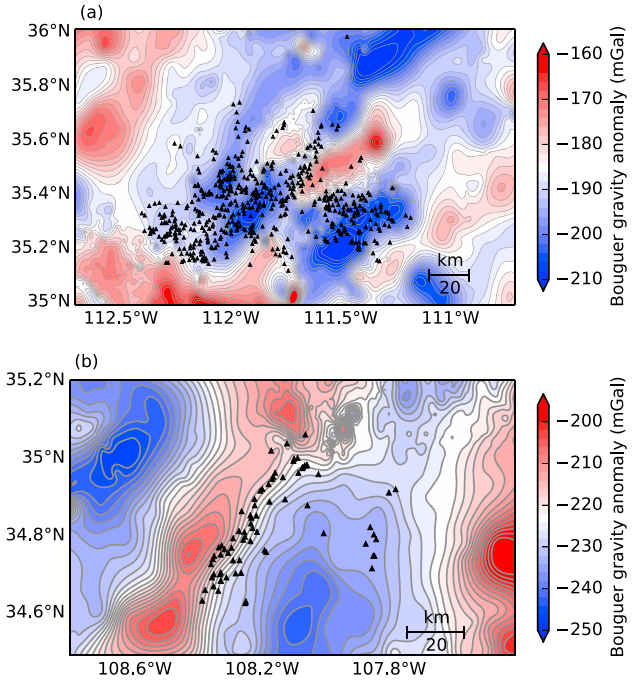

Figure 6. Complete Bouguer gravity anomaly maps of the (a) San Francisco and (b) Zuni-Bandera volcanic fields. Like in the SVF, Quaternary volcanic vents (black triangles) in these two fields are distributed at areas of low gravity anomalies and steep gravity gradients. See Figure 1a for the locations of these volcanic fields. Gravity data are provided by the UTEP database; contour interval is 2 mGal.

continental accretion. Regardless, the density contrasts modeled are consistent with accretion of heterogeneous (mafic and silicic) crust.

In our numerical model, the Proterozoic crust acts as a filter, changing magma ascent pathways. The lateral discontinuities in the crustal density provide rheological boundaries impacting magma ascent. High crustal density may relate to high crustal rigidity, arresting magma ascent on average, over geological time. Based on these results, it is very likely that large-scale crustal structures, such as inherited tectonic block boundaries, influence magma ascent and the clustering of volcanic vents in some distributed volcanic fields.

We looked at vent distributions in two other volcanic fields on the Colorado Plateau, the San Francisco and Zuni-Bandera volcanic fields (Figures 6a and 6b) to search for evidence that crustal structures formed during the Proterozoic influence the clustering of Quaternary-aged volcanic vents. The SFVF is characterized by several NE-SW trending gravity anomalies. Strikingly, two large vent clusters are separated by a NE-SW band of anomalously high gravity (Figure 6a). Like in the SVF, high vent density in the SFVF occurs in areas of anomalously low gravity and large gravity gradient. In the Zuni-Bandera volcanic field, volcanoes are distributed in a NE-trending band (Figure 6b). The highest vent density coincides with the steepest gravity gradient between dense crust to the NW and less dense crust to the SE, where additional volcanoes are located. Thus, the relationship between steep gravity gradients and vent clustering observed in the SVF persists in at least two other Colorado Plateau volcanic fields.

Figures 7a–7d show a simplified model of how a crustal boundary might result in clustered volcanism by altering magma transport, if high crustal density corresponds to low vertical diffusivity. Even if the center of the magma source is relatively far from the crustal boundary and totally beneath the low-diffusivity crust (Figure 7b), the maximum in the simulated surface magma flux is very close (2–3 km) to the crustal boundary and is on the side of high vertical diffusivity (low crustal density). This seems to be the case in the Zuni-Bandera volcanic field. High vent density parallels the steepest gravity gradient, with relatively more vents on the side of low gravity anomaly. Thus, there is evidence from gravity data that the crust acts as a filter changing the pathways of magma ascent. Simulated surface magma flux is relatively high where crustal density is low and especially adjacent to crustal boundaries. We found that it is necessary to remap the crustal density into vertical diffusivity to model the change of magma flux (Figure S9 in the supporting information). Crustal density alone cannot explain the vent clustering observed in these volcanic fields. The variation in diffusivity redirects the ascending magma. For example, in Figure 7d the magma source region is located completely below low-density crust (high-diffusivity crust). Nevertheless, the maximum simulated surface magma flux is located about 3 km away (horizontally) from the center of the magma source, displaced several kilometers toward the crustal boundary.

For now our model is in steady state, taking the integration of volcanism at the surface to simulate the variation in magma flux only in space. A time-transient model might also be used to simulate vent clustering in both space and time. There is a slight decrease in the ages of volcanic vents from west to east in the SVF, suggesting that volcanism migrates due to the motion of the North American Plate relative to a fixed mantle source (Condit et al., 1989). Connor et al. (1992) suggest that the vent migration pattern is complicated by additional factors, including regional structure. It has also been suggested that the absolute westward motion of the North American Plate caused the eastward drift of volcanic activity in the SFVF (Tanaka et al., 1986). Therefore, one could attempt to simulate the evolution of surface magma in the SFVF using a magma source changing with time and a fixed lithosphere to represent the westward motion of the North American Plate. We point out, however, that this effort awaits additional radiometric age determinations of volcanic events in Colorado Plateau volcanic fields. The vast majority of volcanoes are undated as yet, hampering assessment of spatiotemporal models.

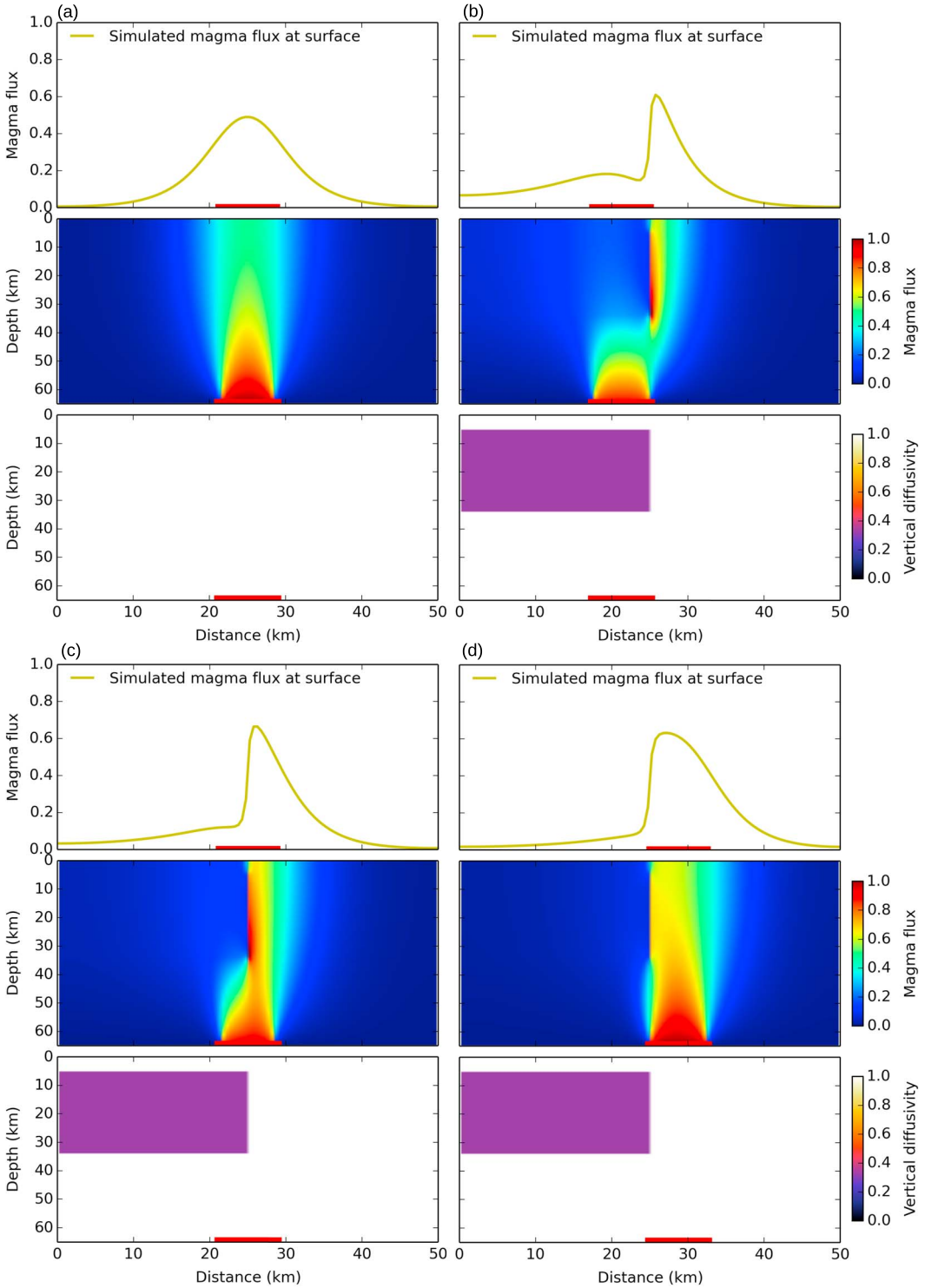

Figure 7. A simplified model showing how average magma flux at the surface is influenced by a crustal boundary and by magma source location (red line on the horizontal axis). (a) Simulated magma flux with homogeneous lithosphere. The maximum in simulated magma flux is exactly above the source center. (b–d) Magma flux is enhanced adjacent to a block of low-diffusivity crust (purple), changing the expected spatial density of volcanic vents. In Figures 7b–7d the position of the magma source region is changed with respect to the crustal boundary, influencing the shape of the calculated magma flux profile at the surface and its position with respect to the center of the magma source region.

7. Conclusions

The complete Bouguer gravity anomaly map of the SVF is refined by our new gravity data. Steep gravity gradients crosscut the volcanic field, and some volcano vent alignments parallel these steep gravity gradients. The long-wavelength gravity anomalies are interpreted as lateral density discontinuities within the Proterozoic crust, and these changes are mapped by inverting gravity data. The spatial density of volcanic vents is greatest is areas of relatively low crustal density located adjacent to high-density areas, suggesting that the structure of the Proterozoic crust influences Quaternary magma ascent.

2-d and 3-D numerical models are developed to simulate long-term average magma migration leading to the development of vent clusters in the SVF. With a uniform magma source, model diffusivity, which is constrained by the density contrast, controls the simulated magma pathways through the lithosphere and magma flux at the surface. Comparing the vent density with simulated surface magma flux, we find that vent distribution is explained by changes in diffusivity associated with the Proterozoic crust. Like the SVF, high vent density in the San Francisco and Zuni-Bandera volcanic fields correspond to low gravity anomalies adjacent to steep gravity gradients. We interpret this correlation to mean that variation in diffusivity redirects the ascending magma. The implication is that in some distributed volcanic fields large-scale crustal structures, such as inherited tectonic block boundaries, influence magma ascent and the clustering of volcanic vents. Probabilistic models of long-term volcanic hazard assessments can be improved by identifying crustal structures and assessing their impact on volcano distribution with the use of numerical models.

Acknowledgments
The research was supported by the National Science Foundation (award 1347899). Part of the field work was supported by the Fred L. and Helen M. Tharp Endowed Scholarship Fund from the University of South Florida. The new gravity data are available in the supporting information. We would like to thank Maurizio Bonafede for his careful and constructive comments on an earlier version of this paper. Thanks also go to editor Paul Tregoning for his patience, encouragement, and feedback.

References

Addington, E. A. (2001). A stratigraphic study of small volcano clusters on Venus. *Icarus*, *149*(1), 16–36.

Aldrich, M. J., & Laughlin, A. W. (1984). A model for the tectonic development of the southeastern Colorado Plateau boundary. *Journal of Geophysical Research*, *89*(B12), 10,207–10,218.

Anderson, J. L., Bender, E. E., Anderson, R. R., Bauer, P. W., Robertson, J. M., Bowring, S. A., … Mawer, C. K. (1993). Transcontinental Proterozoic provinces. In W. R. Van Schmus & M. E. Bickford (Eds.), *The Geology of North America, Volume C-2, Precambrian: Conterminous U.S.* (pp. 171–334). Boulder, CO: The Geological Society of America.

Aubele, J. C., Crumpler, L. S., & Shafiqullah, M. (1986). K-Ar ages of late Cenozoic rocks of the central and eastern parts of the Springerville volcanic field, Arizona. *Isochron/West*, *46*, 3–5.

Awdankiewicz, M., Rapprich, V., & Míková, J. (2016). Magmatic evolution of compositionally heterogeneous monogenetic Cenozoic Strzelin volcanic field (fore-Sudetic block, SW Poland. *Journal of Geosciences*, *61*, 425–450.

Bacon, C. R. (1982). Time-predictable bimodal volcanism in the Coso Range, California. *Geology*, *10*(2), 65–69.

Bebbington, M. S. (2013). Assessing spatio-temporal eruption forecasts in a monogenetic volcanic field. *Journal of Volcanology and Geothermal Research*, *252*, 14–28.

Blakely, R. J. (1996). *Potential theory in gravity and magnetic applications*. Cambridge, UK: Cambridge University Press.

Bonafede, M., & Boschi, E. (1992). A porous-flow model of flank eruptions on Mount Etna. *Journal of Volcanology and Geothermal Research*, *49*(3–4), 349–363.

Bonafede, M., & Cenni, N. (1998). A porous flow model of magma migration within Mt. Etna: The influence of extended sources and permeability anisotropy. *Journal of Volcanology and Geothermal Research*, *81*(1), 51–68.

Cappello, A., Neri, M., Acocella, V., Gallo, G., Vicari, A., & Del Negro, C. (2012). Spatial vent opening probability map of Etna volcano (Sicily, Italy). *Bulletin of Volcanology*, *74*(9), 2083–2094.

Cas, R. A. F., van Otterloo, J., Blaikie, T. N., & van den Hove, J. (2016). The dynamics of a very large intra-plate continental basaltic volcanic province, the Newer Volcanics Province, SE Australia, and implications for other provinces. *Geological Society, London, Special Publications*, *446*, SP446–8.

Condit, C. (1984). The geology of the western part of the Springerville volcanic field, east-central Arizona (PhD thesis), University of New Mexico, Albuquerque, New Mexico.

Condit, C. D., & Connor, C. B. (1996). Recurrence rate of basaltic volcanism in volcanic fields: An example from the Springerville Volcanic Field, AZ, USA. *Geological Society of America, Bulletin*, *108*, 1225–1241.

Condit, C. D., & Shafiqullah, M. (1985). K-Ar ages of late Cenozoic rocks of the western part of the Springerville volcanic field, east-central Arizona. *Isochron/West*, *44*, 3–5.

Condit, C. D., Crumpler, L. S., Aubele, J. C., & Elston, W. E. (1989). Patterns of volcanism along the southern margin of the Colorado Plateau: The Springerville field. *Journal of Geophysical Research*, *94*(B6), 7975–7986.

Connor, C. B. (1990). Cinder cone clustering in the TransMexican volcanic belt: Implications for structural and petrologic models. *Journal of Geophysical Research*, *95*(B12), 19,395–19,405.

Connor, C. B., & Connor, L. J. (2009). Estimating spatial density with kernel methods. In C. B. Connor, N. A. Chapman & L. J. Connor (Eds.), *Volcanic and tectonic hazard assessment for nuclear facilities* (pp. 331–343). Cambridge, UK: Cambridge University Press.

Connor, C. B., & Hill, B. E. (1995). Three nonhomogeneous Poisson models for the probability of basaltic volcanism: Application to the Yucca Mountain region. *Journal of Geophysical Research*, *100*(B6), 10,107–10,125.

Connor, C. B., Condit, C. D., Crumpler, L. S., & Aubele, J. C. (1992). Evidence of regional structural controls on vent distribution, Springerville volcanic field, Arizona. *Journal of Geophysical Research*, *97*, 12,349–12,259.

Connor, L. J., Connor, C. B., Meliksetian, K., & Savov, I. (2012). Probabilistic approach to modeling lava flow inundation: A lava flow hazard assessment for a nuclear facility in Armenia. *Journal of Applied Volcanology*, *1*(1), 3. https://doi.org/10.1186/2191-5040-1-3

Conway, M. F., Ferrill, D. A., Hall, C. M., Morris, A. P., Stamatakos, J. A., Connor, C. B., … Condit, C. (1997). Timing of basaltic volcanism along the Mesa Butte fault zone in the San Francisco volcanic field, Arizona, from $^{40}Ar/^{39}Ar$ ages: Implications for longevity of cinder cone alignments. *Journal of Geophysical Research*, *102*, 815–824.

Conway, M. F., Connor, C. B., Hill, B. E., Condit, C. D., Mullaney, K., & Hall, C. M. (1998). Recurrence rates of basaltic volcanism in the SP cluster, San Francisco volcanic field, Arizona. *Geology*, *26*, 655–658.
Cooper, J. L., & Hart, W. K. (1990). Mantle sources in the Arizona transition zone and global mantle heterogeneity. *Geology*, *18*(11), 1146–1149.
Crow, R., Karlstrom, K., Asmerom, Y., Schmandt, B., Polyak, V., & DuFrane, S. A. (2011). Shrinking of the Colorado Plateau via lithospheric mantle erosion: Evidence from Nd and Sr isotopes and geochronology of Neogene basalts. *Geology*, *39*(1), 27–30.
Crumpler, L. S., Aubele, J. C., & Condit, C. D. (1994). Volcanoes and neotectonic characteristics of the Springerville volcanic field, Arizona. In *Mogollon Slope, west-central New Mexico and east-central Arizona: New Mexico Geological Society 45th Field Conference* (pp. 147–164). West-Central New Mexico and East-Central Arizona: Mogollon Slope.
Dixon, J. E., Dixon, T. H., Bell, D. R., & Malservisi, R. (2004). Lateral variation in upper mantle viscosity: Role of water. *Earth and Planetary Science Letters*, *222*(2), 451–467.
Doherty, J. (2016). PEST, Model-Independent Parameter Estimation User Manual Part I: PEST, SENSAN and Global Optimisers (6th ed.). Brisbane, Australia: Watermark Numerical Computing. Retrieved from http://www.pesthomepage.org/getfiles.php?file=newpestman1.pdf
Duong, T. (2007). ks: Kernel density estimation and kernel discriminant analysis for multivariate data in R. *Journal of Statistical Software*, *21*(7), 1–16.
Farr, T. G., Rosen, P. A., Caro, E., Crippen, R., Duren, R., Hensley, S., … Seal, D. (2007). The Shuttle Radar Topography Mission. *Reviews of Geophysics*, *45*, RG2004. https://doi.org/10.1029/2005RG000183
George, O. A., Malservisi, R., Govers, R., Connor, C. B., & Connor, L. J. (2016). Is uplift of volcano clusters in the Tohoku Volcanic Arc, Japan, driven by magma accumulation in hot zones? A geodynamic modeling study. *Journal of Geophysical Research: Solid Earth*, *121*, 4780–4796. https://doi.org/10.1002/2016JB012833
Germa, A., Connor, L. J., Canon-Tapia, E., & LeCorvec, N. (2013). Spatial distribution of monogenetic eruptive vents from volcanic fields in central Baja California, Mexico. *Bulletin of Volcanology*, *75*(12), 1–14.
Gilbert, H., Velasco, A. A., & Zandt, G. (2007). Preservation of Proterozoic terrane boundaries within the Colorado Plateau and implications for its tectonic evolution. *Earth and Planetary Science Letters*, *258*(1), 237–248.
Hammer, S. (1939). Terrain corrections for gravimeter stations. *Geophysics*, *4*(3), 184–194.
Harbaugh, A. W. (2005). *MODFLOW-2005, the US Geological Survey modular ground-water model: The ground-water flow process*. Reston, VA: U.S. Department of the Interior, U.S. Geological Survey.
Hasenaka, T., & Carmichael, I. S. E. (1985). The cinder cones of Michoacán–Guanajuato, central Mexico: Their age, volume and distribution, and magma discharge rate. *Journal of Volcanology and Geothermal Research*, *25*(1–2), 105–124.
Heidbach, O., Tingay, M., Barth, A., Reinecker, J., Kurfeß, D., & Müller, B. (2010). Global crustal stress pattern based on the World Stress Map database release 2008. *Tectonophysics*, *482*(1), 3–15.
Heming, R. F. (1980). Patterns of Quaternary basaltic volcanism in the northern North Island, New Zealand. *New Zealand Journal of Geology and Geophysics*, *23*(3), 335–344.
Hinze, W. J. (2003). Bouguer reduction density, why 2.67? *Geophysics*, *68*(5), 1559–1560.
Humphreys, E., Hessler, E., Dueker, K., Farmer, G. L., Erslev, E., & Atwater, T. (2003). How Laramide-age hydration of North American lithosphere by the Farallon slab controlled subsequent activity in the western United States. *International Geology Review*, *45*(7), 575–595.
Humphreys, E. D. (1995). Post-Laramide removal of the Farallon slab, western United States. *Geology*, *23*(11), 987–990.
Jaquet, O., & Carniel, R. (2006). Estimation of volcanic hazards using geostatistical models. In H. Mader, S. Coles, C. B. Connor & L. J. Connor (Eds.), *Statistics in volcanology* (pp. 89–103). no. 1 in Special Publications of IAVCEI. London, UK: Geological Socierty of London.
Karlstrom, K. E., & Bowring, S. A. (1988). Early Proterozoic assembly of tectonostratigraphic terranes in southwestern North America. *The Journal of Geology*, *96*(5), 561–576.
Karlstrom, K. E., & Williams, M. L. (2006). Nature and evolution of the middle crust—Heterogeneity of structure and process due to pluton-enhanced tectonism. In M. Brown & T. Rushmer (Eds.), *Evolution and differentiation of the continental crust* (pp. 268–295). Cambridge, UK: Cambridge University Press.
Kavanagh, J. L., Menand, T., & Sparks, R. S. J. (2006). An experimental investigation of sill formation and propagation in layered elastic media. *Earth and Planetary Science Letters*, *245*(3), 799–813.
Kereszturi, G., & Németh, K. (2016). Sedimentology, eruptive mechanism and facies architecture of basaltic scoria cones from the Auckland Volcanic Field (New Zealand). *Journal of Volcanology and Geothermal Research*, *324*, 41–56.
Kiyosugi, K., Connor, C. B., Zhao, D., Connor, L. J., & Tanaka, K. (2010). Relationships between volcano distribution, crustal structure, and P-wave tomography: An example from the Abu Monogenetic Volcano Group, SW Japan. *Bulletin of Volcanology*, *72*(3), 331–340.
LaFehr, T. R. (1991). An exact solution for the gravity curvature (Bullard B) correction. *Geophysics*, *56*(8), 1179–1184.
Laughlin, A. W., Damon, P. E., & Shafiquallah, M. (1980). New K–Ar dates from the Springerville volcanic field, central Jemez zone, Apache county, Arizona. *Isochron/West*, *29*, 3–4.
Leandro, R., Landau, H., Nitschke, M., Glocker, M., Seeger, S., Chen, X., & Kipka, A. (2011). RTX positioning: The next generation of cm-accurate real-time GNSS positioning. In *Proceedings of the 24th International Technical Meeting of The Satellite Division of the Institute of Navigation (ION GNSS 2011)* (pp. 1460–1475). Portland, OR.
Le Corvec, N., Spörli, K. B., Rowland, J., & Lindsay, J. (2013). Spatial distribution and alignments of volcanic centers: Clues to the formation of monogenetic volcanic fields. *Earth Science Reviews*, *124*, 96–114.
Levander, A., Schmandt, B., Miller, M. S., Liu, K., Karlstrom, K. E., Crow, R. S., … Humphreys, E. D. (2011). Continuing Colorado Plateau uplift by delamination-style convective lithospheric downwelling. *Nature*, *472*(7344), 461–465.
Liu, K., Levander, A., Niu, F., & Miller, M. S. (2011). Imaging crustal and upper mantle structure beneath the Colorado Plateau using finite frequency Rayleigh wave tomography. *Geochemistry, Geophysics, Geosystems*, *12*, Q07001. https://doi.org/10.1029/2011GC003611
Luedke, R. G., & Smith, R. L. (1978). Map showing distribution, composition, and age of late Cenozoic volcanic centers in Arizona and New Mexico, IMAP 1091-A, U.S. Geological Survey Publication. Retrieved from http://pubs.er.usgs.gov/publication/i1091A
Maccaferri, F., Bonafede, M., & Rivalta, E. (2010). A numerical model of dyke propagation in layered elastic media. *Geophysical Journal International*, *180*(3), 1107–1123.
Maccaferri, F., Bonafede, M., & Rivalta, E. (2011). A quantitative study of the mechanisms governing dike propagation, dike arrest and sill formation. *Journal of Volcanology and Geothermal Research*, *208*(1), 39–50.
Mazzarini, F., Corti, G., Manetti, P., & Innocenti, F. (2004). Strain rate and bimodal volcanism in the continental rift: Debre Zeyt volcanic field, northern MER, Ethiopia. *Journal of African Earth Sciences*, *39*(3), 415–420.

Nakamura, K. (1977). Volcanoes as possible indicators of tectonic stress orientation—Principle and proposal. *Journal of Volcanology and Geothermal Research*, *2*(1), 1–16.
Nealey, L. D. (1989). Field trip road log for the White Mountain volcanic field, southeastern Colorado Plateau. In C. Chapin & J. Zidek (Eds.), *Field excursions to volcanic terrains in the western United States, volume 1, Southern Rocky Mountain Region, Memoir 46* (pp. 221–225): Socorro, NM: New Mexico Bureau of Geology & Mineral Resources. Retrieved from https://geoinfo.nmt.edu/publications/monographs/memoirs/46/
Peirce, H. W., Damon, P. E., & Shafiquallah, M. (1979). An Oligocene (?) Colorado Plateau edge in Arizona. *Tectonophysics*, *61*, 1–24.
Putirka, K., & Condit, C. D. (2003). Cross section of a magma conduit system at the margin of the Colorado Plateau. *Geology*, *31*(8), 701–704.
Richardson, J. A., Bleacher, J. E., & Glaze, L. S. (2013). The volcanic history of Syria Planum, Mars. *Journal of Volcanology and Geothermal Research*, *252*, 1–13.
Rittmann, A. (1962). *Volcanoes and their activity*, (p. 305). New York: John Wiley.
Schmincke, H. U., Lorenz, V., & Seck, H. A. (1983). The quaternary Eifel volcanic fields. In *Plateau uplift* (pp. 139–151). Germany: Springer, Berlin.
Schwartz, F. W., & Zhang, H. (2003). *Fundamentals of groundwater* (p. 583). New York: John Wiley.
Seeley, J. M., & Keller, G. R. (2003). Delineation of subsurface Proterozoic Unkar and Chuar Group sedimentary basins in northern Arizona using gravity and magnetics: Implications for hydrocarbon source potential. *AAPG Bulletin*, *87*(8), 1299–1321.
Shoemaker, E. M., Squires, R. L., & Abrams, M. J. (1978). Bright Angel and Mesa Butte fault systems of northern Arizona. *Geological Society of America Memoirs*, *152*, 341–367.
Sugarbaker, L. J., Eldridge, D. F., Jason, A. L., Lukas, V., Saghy, D. L., Stoker, J. M., & Thuen, D. R. (2017). Status of the 3D elevation program, 2015 (*Open-File Report 2016Ű1196*). U.S. Geological Survey. https://doi.org/10.3133/ofr20161196
Tanaka, K. L., Shoemaker, E. M., Ulrich, G. E., & Wolfe, E. W. (1986). Migration of volcanism in the San Francisco volcanic field, Arizona. *Geological Society of America Bulletin*, *97*(2), 129–141.
Thompson, G. A., & Zoback, M. L. (1979). Regional geophysics of the Colorado Plateau. *Tectonophysics*, *61*(1–3), 149–181.
University of Texas at El Paso (UTEP) database (2017). Gravity Database of the US. El Paso, TX: The University of Texas at El Paso. Retrieved from http://research.utep.edu/default.aspx?tabid=37229
Valentine, G. A., & Connor, C. B. (2015). Chapter 23 - Basaltic Volcanic Fields. In H. Sigurdsson, et al. (Eds.), *The Encyclopedia of Volcanology* (2nd ed., pp. 423–439). Elsevier, Inc: Academic Press.
Van Wijk, J. W., Baldridge, W. S., Van, H. J., Goes, S., Aster, R., Coblentz, D. D. D., … Ni, J. (2010). Small-scale convection at the edge of the Colorado Plateau: Implications for topography, magmatism, and evolution of Proterozoic lithosphere. *Geology*, *38*(7), 611–614.
van den Hove, J. C., van Otterloo, J., Betts, P. G., Ailleres, L., & Cas, R. A. F. (2017). Controls on volcanism at intraplate basaltic volcanic fields. *Earth and Planetary Science Letters*, *459*, 36–47.
Wand, M. P., & Jones, M. C. (1995). *Kernel smoothing*. London: Chapman and Hall.
Wei, H., Sparks, R. S. J., Liu, R., Fan, Q., Wang, Y., Hong, H., … Pan, Y. (2003). Three active volcanoes in China and their hazards. *Journal of Asian Earth Sciences*, *21*(5), 515–526.
Wessel, P., Smith, W. H., Scharroo, R., Luis, J., & Wobbe, F. (2013). Generic mapping tools: Improved version released. *Eos Transactions American Geophysical Union*, *94*(45), 409–410.
Wetmore, P. H., Connor, C. B., Kruse, S. E., Callihan, S., Pignotta, G., Stremtan, C., & Burke, A. (2009). Geometry of the Trachyte Mesa intrusion, Henry Mountains, Utah: Implications for the emplacement of small melt volumes into the upper crust. *Geochemistry, Geophysics, Geosystems*, *10*, Q08006. https://doi.org/10.1029/2009GC002,469
White, J. T., Karakhanian, A., Connor, C. B., Connor, L. J., Hughes, J. D., Malservisi, R., & Wetmore, P. H. (2015). Coupling geophysical investigation with hydrothermal modeling to constrain the enthalpy classification of a potential geothermal resource. *Journal of Volcanology and Geothermal Research*, *298*, 59–70.
Williams, H. (1950). *Volcanoes of the Parícutin Region, Mexico: Geologic Investigations in the Parícutin Area*. Mexico: U.S. Geological Survey.
Zandt, G., & Reiners, P. (2011). Earth science: Lithosphere today … . *Nature*, *472*(7344), 420–421.